

Neural Configuration-Space Barriers for Manipulation Planning and Control

Kehan Long, Ki Myung Brian Lee, Nikola Raicevic, Niyas Attasseri, Melvin Leok, and Nikolay Atanasov

Contextual Robotics Institute

University of California San Diego, La Jolla, CA 92093

Abstract—Planning and control for high-dimensional robot manipulators in cluttered, dynamic environments require both computational efficiency and robust safety guarantees. Inspired by recent advances in learning configuration-space distance functions (CDFs) as robot body representations, we propose a unified framework for motion planning and control that formulates safety constraints as CDF barriers. A CDF barrier approximates the local free configuration space, substantially reducing the number of collision-checking operations during motion planning. However, learning a CDF barrier with a neural network and relying on online sensor observations introduce uncertainties that must be considered during control synthesis. To address this, we develop a distributionally robust CDF barrier formulation for control that explicitly accounts for modeling errors and sensor noise without assuming a known underlying distribution. Simulations and hardware experiments on a 6-DoF xArm manipulator show that our neural CDF barrier formulation enables efficient planning and robust real-time safe control in cluttered and dynamic environments, relying only on onboard point-cloud observations.

I. INTRODUCTION

Efficient planning and safe control for high-degree-of-freedom (DoF) robotic manipulators are a central challenge in robotics, particularly when operating in cluttered and dynamic environments with noisy sensor measurements. Sampling-based motion planners, such as rapidly-exploring random trees (RRT) [27, 43] and probabilistic roadmaps (PRM) [23], have gained widespread adoption for manipulator motion planning because they effectively explore high-dimensional spaces without exhaustive configuration-space discretization. Despite their strengths, these methods rely on frequent collision checks, making the efficiency and accuracy of collision checking a critical bottleneck. Moreover, in highly dynamic settings with sensor noise and rapidly changing obstacles, planning alone is insufficient to ensure safety during execution, promoting the integration of robust real-time control strategies.

To address these challenges, signed distance functions (SDFs) have gained popularity for encoding the distance from any point in the workspace to the boundary of an object, thereby enabling precise collision checks and facilitating gradient-based optimization. Recently, neural networks have been leveraged to learn SDF representations of both environments [36, 40, 32] and robot bodies [25, 30, 47], providing rich shape modeling along with efficient distance and gradient queries. Building on these advancements, neural SDFs have been adopted in motion planning [47, 37] and optimization-based safe control [32, 39], yielding promising

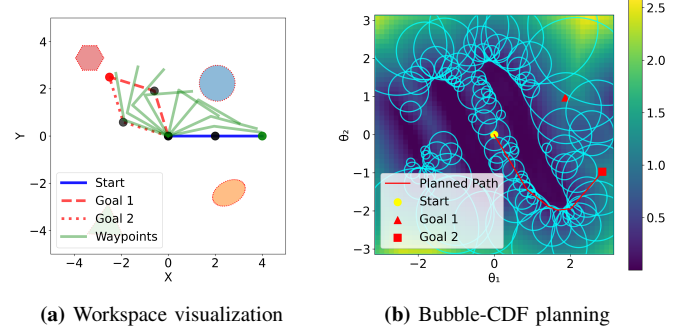


Fig. 1: Illustration of neural bubble-CDF planning on a planar 2-link robot arm. (a) The robot’s initial configuration (solid blue links) and two potential goal configurations (dashed red) are shown. Four obstacles with point-cloud data on their surfaces define the environment, and intermediate waypoints of the bubble-CDF planned trajectory appear in light green. (b) The 2D configuration space (θ_1 vs. θ_2) for a planar 2-link robot, where the color map indicates the learned CDF value (darker regions denote proximity to collision). Cyan circles represent “safe bubbles” derived from the CDF barrier, forming a graph of collision-free regions. A smooth, optimized red trajectory connects the start configuration (yellow circle) to the closest goal (red square), while another goal configuration is marked by a red triangle.

results in complex, dynamic scenarios.

While SDFs have proven effective in workspace-centric tasks, such as planning and obstacle avoidance for mobile robots [35, 32], recent work [29] demonstrates that directly representing distances in configuration space can be particularly advantageous for manipulators with high-dimensional kinematic chains. In a *configuration distance field* (CDF), the distance is measured in joint space between a given configuration and a workspace point, eliminating the need for repeated transformations between task and configuration spaces. Like neural SDFs, neural CDFs offer a compact and differentiable representation, supporting efficient gradient-based computations for real-time motion planning [29] and reactive control [7]. However, learning-based representations inevitably introduce modeling errors, and real-world deployments must also contend with sensor noise and other uncertainties.

Motivated by these challenges, we propose an approach that integrates a neural CDF barrier into both motion planning and control, addressing the twin requirements of computational efficiency and safety under uncertainty. The **contributions** of this work are summarized as follows.

- We introduce a unified neural CDF barrier formulation that estimates the configuration-space distance to both environment obstacles and self-collisions. This is achieved

by separately learning an environment CDF and a self-collision CDF for high-DoF manipulators. The resulting barrier enables efficient and scalable safety evaluation based on point-cloud observations.

- We develop the bubble-CDF motion planning algorithm, which constructs a graph of fully traversable configuration-space bubbles using the neural CDF barrier. This approach significantly reduces the number of collision checks and achieves faster planning times compared to traditional sampling-based planners.
- We propose a distributionally robust control barrier function (DR-CBF) formulation based on the neural CDF barrier, which accounts for dynamic obstacles, modeling errors, and perception uncertainty.
- We validate the proposed framework in both simulation and real-robot experiments with a 6-DoF xArm manipulator operating in dynamic and cluttered environments, demonstrating improved efficiency and safety.

II. RELATED WORK

This section reviews existing approaches for motion planning and control of robotic manipulators.

To plan and execute manipulator motions, the prevailing approach is to use discrete sampling-based planners such as RRT [27], PRM [23], and their variants [26, 19] to compute a global path in the configuration space, which is then followed using feedback controllers such as PID [22]. These methods have been widely adopted due to their simplicity and ability to generate collision-free paths in complex environments. However, as manipulators are deployed in increasingly dynamic and unstructured environments, the limitations of sampling-based planners become evident, particularly their reliance on computationally expensive collision checking, which restricts frequent replanning, and their inability to adapt paths in real-time, leading to potential safety risks during execution.

To address the challenges associated with frequent collision checking, a line of work focuses on constructing explicit approximations of the free configuration space. Methods of Dai et al. [9], Werner et al. [44], Deits and Tedrake [11] decompose the free configuration space into multiple convex polyhedra by solving a series of optimization problems, typically assuming that workspace obstacles are represented by geometric primitives such as spheres or cylinders. Some prior works, such as Ademovic and Lacevic [1], Danielson [10], utilize workspace distances to construct safe regions; however, these methods are restricted to simple manipulator geometries, such as infinitely thin lines. Additionally, spherical safe regions have been explored for efficient collision checking [5, 38], biased sampling in free workspace representations [6], and navigation function design [45]. Our approach differs by using these regions as convex constraints for trajectory optimization in configuration space, extending the concept introduced by Lee et al. [28] to high-dimensional robot configurations and more complex environments.

Accurate geometric modeling is essential for enabling manipulators to safely navigate complex and dynamic environ-

ments. Signed distance functions (SDFs) have been extensively utilized in manipulator motion planning and control due to their efficient computation of distances and gradients [25, 13, 47, 30]. Koptev et al. [25] introduced neural joint SDFs to facilitate collision-free motion planning for manipulators, while Vasilopoulos et al. [42] leveraged manipulator SDFs for reactive motion planning by integrating a model predictive path integral trajectory generator with a vector field-based follower. From a safety-critical perspective, Singletary et al. [39] proposed a CBF-based trajectory filtering strategy that dynamically adjusts pre-planned manipulator trajectories to account for updated collision constraints. Yu et al. [46] developed a CBF-induced neural controller (CBF-INC) that integrates with RRT for motion planning, utilizing state-based or point-cloud inputs to enhance success rates and reduce exploration nodes.

Recent advancements have extended the utility of distance fields to configuration space for manipulators. Li et al. [29] introduced the concept of a configuration distance field (CDF) and proposed using a neural network to approximate it, allowing the estimation of the joint space distance between a given configuration and a workspace point. Building on this, Chi et al. [7] leveraged neural CDFs as control barrier functions (CBFs) for safe control, demonstrating that CDF-based methods outperform SDF-based approaches due to their more reliable gradient estimates.

While Chi et al. [7] is closely related to this work, we differ in several key aspects. First, we extend the application of neural CDFs to both planning and control frameworks, addressing the dual objectives of planning efficiency and safety under uncertainty. Specifically, our planning strategy leverages configuration-space bubbles constructed with neural CDF barriers, enabling efficient exploration and trajectory optimization. Second, our control formulation explicitly accounts for the modeling errors inherent in neural approximations and sensor measurement uncertainties by incorporating a distributionally robust formulation. These enhancements enable our framework to provide robust and reliable performance in dynamic and cluttered environments while relying on point-cloud sensory measurements.

III. PROBLEM FORMULATION

We consider a robot manipulator with m revolute joints and $m + 1$ links, where Link 0 denotes the fixed base. The joint configuration is represented by $\mathbf{q} = [q_1, \dots, q_m]^\top \in \mathcal{Q}$, where $\mathcal{Q} = \{\mathbf{q} \in \mathbb{R}^m \mid \mathbf{q}_{\min} \leq \mathbf{q} \leq \mathbf{q}_{\max}\}$ is the configuration space bounded by the joint limits. The forward kinematics of

⁰**Notation:** The sets of real, non-negative real, and natural numbers are denoted by \mathbb{R} , $\mathbb{R}_{\geq 0}$, and \mathbb{N} , respectively. For $N \in \mathbb{N}$, we let $[N] := \{1, 2, \dots, N\}$. The interior and boundary of a set $C \subset \mathbb{R}^n$ are denoted by $\text{Int}(C)$ and ∂C . The gradient of a differentiable function $V : \mathbb{R}^n \rightarrow \mathbb{R}$ is denoted by ∇V . A continuous function $\alpha : \mathbb{R} \rightarrow \mathbb{R}$ is of extended class \mathcal{K}_∞ if it is strictly increasing, $\alpha(0) = 0$, and $\lim_{r \rightarrow \infty} \alpha(r) = \infty$. The special orthogonal group of dimension p is denoted by $\text{SO}(p) = \{\mathbf{R} \in \mathbb{R}^{p \times p} \mid \mathbf{R}^\top \mathbf{R} = \mathbf{I}_p, \det(\mathbf{R}) = 1\}$. The special Euclidean group of dimension p , denoted $\text{SE}(p)$ is the set of matrices $\begin{pmatrix} \mathbf{R} & \mathbf{t} \\ \mathbf{0}^\top & 1 \end{pmatrix}$ with $\mathbf{R} \in \text{SO}(p)$, $\mathbf{t} \in \mathbb{R}^p$.

the manipulator map a joint configuration \mathbf{q} to the end-effector pose in task space, represented as $\mathbf{T}_{ee}(\mathbf{q}) \in \text{SE}(3)$.

Given a configuration \mathbf{q} , we denote the robot shape by a set-valued function $\mathcal{S}(\mathbf{q}) \subset \mathbb{R}^3$, and its surface by $\partial\mathcal{S}(\mathbf{q})$. The kinematics of the manipulator are described by:

$$\dot{\mathbf{q}}(t) = \mathbf{u}(t), \quad \mathbf{q}(0) = \mathbf{q}_0, \quad (1)$$

where $\mathbf{u} \in \mathcal{U} \subset \mathbb{R}^m$ is the joint velocity control input, and \mathbf{q}_0 is the initial configuration of the robot.

We consider a dynamic environment containing both static and dynamic obstacles. At time t , let $\mathcal{O}(t) \subset \mathbb{R}^3$ denote the closed set of obstacles, and let the free space be represented as $\mathcal{F}(t) = \mathbb{R}^3 \setminus \mathcal{O}(t)$, which is an open set. We assume that a sensor (e.g., depth camera or LiDAR) provides point-cloud measurements $\mathcal{P}(t) \subset \mathbb{R}^3$, which approximate the boundary of the time-varying obstacle region $\mathcal{O}(t)$. The extrinsic parameters relating the sensor pose to the robot base are assumed to be calibrated offline.

Problem 1. Consider a robot manipulator with initial configuration \mathbf{q}_0 and dynamics in (1). Given point-cloud observations $\mathcal{P}(t)$ of the obstacles $\mathcal{O}(t)$ in the environment, design a control policy that drives the robot's end-effector \mathbf{T}_{ee} to a desired goal pose $\mathbf{T}_G \in \text{SE}(3)$, while ensuring the robot body remains in free space, i.e., $\mathcal{S}(\mathbf{q}(t)) \subset \mathcal{F}(t)$, $\forall t \geq 0$.

IV. SAFE BARRIER FROM CONFIGURATION-SPACE DISTANCE FUNCTION

Efficient motion planning and control for robotic manipulators require accurate and scalable safety representations in configuration space. In this section, we first review the notion of a signed distance function (SDF) in the workspace, then introduce the environment and self-collision CDF and their key properties, and finally define a neural CDF barrier for planning and control applications.

A. Environment Configuration Space Distance Function

Motivated by successful applications in safe mobile robot navigation [17, 32, 24], SDFs have recently been used for motion planning and control of robot manipulators [25, 30, 46, 33]. An SDF f_s measures the distance from a workspace point $\mathbf{p} \in \mathbb{R}^3$ to the robot surface $\partial\mathcal{S}(\mathbf{q})$:

$$f_s(\mathbf{p}, \mathbf{q}) = \begin{cases} -\min_{\mathbf{p}^* \in \partial\mathcal{S}(\mathbf{q})} \|\mathbf{p} - \mathbf{p}^*\|, & \text{if } \mathbf{p} \in \mathcal{S}(\mathbf{q}), \\ \min_{\mathbf{p}^* \in \partial\mathcal{S}(\mathbf{q})} \|\mathbf{p} - \mathbf{p}^*\|, & \text{if } \mathbf{p} \notin \mathcal{S}(\mathbf{q}). \end{cases} \quad (2)$$

When represented using a differentiable model (e.g., neural network [36, 25]), this function enables efficient motion planning and collision avoidance by facilitating rapid computation of distances and gradients. While SDFs are widely applied to mobile robots to enforce workspace safety constraints, manipulators with high-dimensional joint spaces benefit from a configuration-centric perspective.

Li et al. [29] introduced a configuration distance function (CDF), which encodes the minimum joint-space distance (in radians) needed for a robot at configuration \mathbf{q} to make contact

with a point \mathbf{p} . Formally, given a robot SDF f_s , the robot CDF can be computed as

$$f_c(\mathbf{p}, \mathbf{q}) = \min_{\mathbf{q}'} \|\mathbf{q} - \mathbf{q}'\|, \quad \text{subject to } f_s(\mathbf{p}, \mathbf{q}') = 0. \quad (3)$$

Similar to an SDF, this CDF representation satisfies an Eikonal equation with respect to \mathbf{q} :

$$\|\nabla_{\mathbf{q}} f_c(\mathbf{p}, \mathbf{q})\| = 1, \quad (4)$$

whenever it is differentiable in \mathbf{q} .

In practice, computing (3) requires identifying a set of zero-level configurations \mathbf{q}' satisfying $f_s(\mathbf{p}, \mathbf{q}') = 0$. These configurations are typically obtained using numerical optimization methods such as Broyden-Fletcher-Goldfarb-Shanno (BFGS) algorithm [20]. However, due to the high dimensionality of the configuration space and the sparsity of \mathbf{q}' samples, this direct formulation can lead to an overly smooth or inaccurate approximation of the true CDF. Therefore, Li et al. [29] leverage the fact that the contact at a point \mathbf{p} is primarily determined by a subset of joints preceding the contact link. Let k denote the robot link that comes into contact with \mathbf{p} , and let $\mathbf{q}_{:k}$ represent the joint angles influencing the motion of link k . The CDF is then refined by restricting the distance computation to these relevant joints:

$$f_c(\mathbf{p}, \mathbf{q}) = \min_{k=1, \dots, m} \min_{\mathbf{q}'} \|\mathbf{q}_{:k} - \mathbf{q}'_{:k}\|, \quad \text{s.t. } f_s(\mathbf{p}, \mathbf{q}') = 0, \quad (5)$$

where m is the total number of robot joints.

B. Self-Collision Configuration Space Distance Function

While environment CDFs measure proximity to external obstacles, self-collisions between different parts of the robot pose a distinct challenge, especially for high-DoF manipulators where self-intersections are configuration-dependent and complex. To address this, we define the *Self-Collision Configuration Distance Function* (SCDF), which quantifies the minimum joint-space distance from a configuration \mathbf{q} to the set of self-colliding configurations.

Let $\mathcal{C}_{sc} \subset \mathcal{Q}$ denote the closed set of joint configurations that result in self-collision. Then, for a given configuration $\mathbf{q} \in \mathcal{Q}$, we define the SCDF as:

$$f_{sc}(\mathbf{q}) := \min_{\mathbf{q}' \in \mathcal{C}_{sc}} \|\mathbf{q} - \mathbf{q}'\|. \quad (6)$$

Similar to Section IV-A, the SCDF in (6) represents the Euclidean distance from \mathbf{q} to the closed set of self-colliding configurations $\mathcal{C}_{sc} \subset \mathbb{R}^m$. Note that \mathcal{C}_{sc} may consist of multiple disconnected components, as different joint subsets can lead to distinct types of self-collision. Nevertheless, the SCDF inherits the Eikonal property and satisfies

$$\|\nabla_{\mathbf{q}} f_{sc}(\mathbf{q})\| = 1. \quad (7)$$

In practice, \mathcal{C}_{sc} is often only sparsely sampled, and self-collisions typically involve only a subset of joints. As such, computing the full-joint distance in (6) can lead to overly conservative and inaccurate approximations. To improve accuracy and better exploit the robot's kinematic structure, we refine the

SCDF by computing distance only over the subset of joints responsible for the self-collision.

Specifically, if a self-collision at \mathbf{q}' occurs between Link i and Link j , we define the joint subvector $\mathbf{q}_{a:b}$, where $a = \min(i, j)$ and $b = \max(i, j)$, to include only joints that affect the relative motion of these links. The refined SCDF becomes:

$$f_{sc}(\mathbf{q}) := \min_{\mathbf{q}' \in \mathcal{C}_{sc}} \|\mathbf{q}_{a:b} - \mathbf{q}'_{a:b}\|. \quad (8)$$

For example, if the collision occurs between Link 3 and Link 5, then joints 3 through 5 may primarily determine their relative positions, so the distance is computed using $\mathbf{q}_{3:5}$.

C. Neural CDF Barrier

Building on the environment and self-collision CDF, we define a CDF barrier to ensure the robot remains in a collision-free region of the configuration space. Formally, a CDF barrier associated with environment CDF f_c , self-collision CDF f_{sc} , and obstacle set $\mathcal{O}(t)$ is defined as:

$$h(\mathbf{q}, t) := \min\left\{\inf_{\mathbf{p} \in \partial\mathcal{O}(t)} f_c(\mathbf{p}, \mathbf{q}), f_{sc}(\mathbf{q})\right\} \quad (9)$$

where $\partial\mathcal{O}(t)$ is the obstacle set boundary. Then, the time-varying *safe set* in configuration space induced by $h(\mathbf{q}, t)$ is

$$\mathcal{C}_{safe}(t) = \{\mathbf{q} \in \mathcal{Q} \mid h(\mathbf{q}, t) \geq 0\}. \quad (10)$$

In real-world settings, $\partial\mathcal{O}(t)$ must be inferred from point-cloud measurements $\mathcal{P}(t)$ from a depth camera or LiDAR. Because the points in $\mathcal{P}(t)$ are noisy samples from the boundary of $\mathcal{O}(t)$, we approximate the CDF barrier as

$$h(\mathbf{q}, t) \approx \min\left\{\min_{\mathbf{p} \in \mathcal{P}(t)} f_c(\mathbf{p}, \mathbf{q}), f_{sc}(\mathbf{q})\right\}. \quad (11)$$

Moreover, computing $f_c(\mathbf{p}, \mathbf{q})$ and $f_{sc}(\mathbf{q})$ exactly are difficult for high-DoF manipulators because it involves (infinitely) many potential contact configurations \mathbf{q}' in (3) and self-collision configurations in (8). Similar to Li et al. [29], we model f_c and f_{sc} by multi-layer perceptrons $\hat{f}_c(\mathbf{p}, \mathbf{q}; \boldsymbol{\theta}_1)$ and $\hat{f}_{sc}(\mathbf{q}; \boldsymbol{\theta}_2)$ with learnable parameters $\boldsymbol{\theta}_1$ and $\boldsymbol{\theta}_2$, respectively. This representation reduces the storage requirements compared to volumetric or tabular encodings and supports parallel queries for a set of points \mathbf{p} or configurations \mathbf{q} with associated gradient computations.

However, learning-based representations inevitably introduce modeling errors. Combining the point-cloud approximation with the neural CDF approximation yields a practical CDF barrier:

$$\hat{h}(\mathbf{q}, t; \boldsymbol{\theta}) = \min\left\{\min_{\mathbf{p} \in \mathcal{P}(t)} \hat{f}_c(\mathbf{p}, \mathbf{q}; \boldsymbol{\theta}_1), \hat{f}_{sc}(\mathbf{q}; \boldsymbol{\theta}_2)\right\} \quad (12)$$

where the noise in $\mathcal{P}(t)$, its lack of complete coverage of the obstacle boundary, and the approximation error in \hat{f}_c and \hat{f}_{sc} constitute multiple sources of uncertainty.

In the following sections, we leverage the fast parallel query capabilities of the neural CDF barrier to enable efficient sampling-based planning in configuration space (Sec. V), and then propose a distributionally robust control strategy that tracks the planned trajectory while ensuring real-time safety despite uncertainties and dynamic obstacles (Sec. VI).

V. CONFIGURATION SPACE BUBBLE-BASED PLANNING

Motion planning for high-DoF manipulators typically involves numerous collision checks [19], making global motion planning computationally expensive. To address this, we propose the **bubble-CDF planner**, a sampling-based approach that efficiently explores the configuration space while ensuring safety via neural CDF barriers. Unlike conventional RRT-based planners that rely on dense edge validation, our approach constructs *configuration space bubbles* as local safe regions, enabling rapid exploration and collision-free path generation.

In Problem 1, the robot must move from an initial configuration \mathbf{q}_0 to any valid joint configuration \mathbf{q}_G that achieves a desired end-effector pose $\mathbf{T}_{ee}(\mathbf{q}_G) = \mathbf{T}_G \in \text{SE}(3)$. Inverse kinematics (IK) provides K goal configurations $\{\mathbf{q}_G^i\}_{i \in [K]}$, each of which achieves the desired end-effector pose.

Our approach builds on the *Rapidly Exploring Bubble Graph (RBG)* algorithm [28], which constructs a configuration-space roadmap where each node represents a locally safe region (bubble) instead of a single configuration. The learned CDF barrier $\hat{h}(\mathbf{q}, t)$ is used to define the bubble radius dynamically, ensuring rapid, collision-free exploration without incremental edge validation. This substantially reduces the collision-checking overhead in high-dimensional spaces while preserving the efficiency of sampling-based planners.

A. Rapidly-exploring Bubble Graph (RBG)

Suppose $\mathbf{q} \in \mathcal{Q}$ is a safe configuration. We aim to identify a radius $r(\mathbf{q}) \geq 0$ such that any configuration \mathbf{q}' satisfying $\|\mathbf{q} - \mathbf{q}'\| \leq r(\mathbf{q})$ is safe. We call this spherical region a *configuration-space bubble* and denote it as $\mathcal{B}(\mathbf{q}, r(\mathbf{q}))$. Given the neural CDF barrier $\hat{h}(\mathbf{q}, t)$ for fixed time t , we construct the bubble radius at configuration \mathbf{q} as:

$$r(\mathbf{q}) = \hat{h}(\mathbf{q}, t) - \eta, \quad (13)$$

where $\eta > 0$ is a safety margin. All configurations \mathbf{q}' within this radius satisfy the neural CDF barrier with margin $h(\mathbf{q}', t) \geq \eta$ [28].

To explore a high-dimensional configuration space efficiently using these local safety certificates, RBG adapts the RRT algorithm [27] so that each vertex in the graph corresponds to a bubble rather than a single configuration. In RBG, the step size, corresponding to the distance the planned tree advances toward a sampled point, is dynamically set by the radius of each bubble. This obviates manual tuning of a fixed step size and reduces collision-checking overhead.

Algorithm 1 details how RBG constructs a bubble-based graph. RBG iteratively samples random configurations (biased toward goal configurations), identifies the nearest bubble in configuration space, and if the sample lies outside that bubble, creates a new bubble by querying the neural CDF barrier to determine its radius. The newly created bubble is then connected to any existing bubbles $\mathcal{B}(\mathbf{q}_i, r(\mathbf{q}_i))$ with overlapping safe regions, i.e., if

$$\|\mathbf{q}_{\text{new}} - \mathbf{q}_i\| \leq r(\mathbf{q}_{\text{new}}) + r(\mathbf{q}_i). \quad (14)$$

Algorithm 1 Rapidly Exploring Bubble Graph

Require: Start configuration \mathbf{q}_0 , goal configurations $\{\mathbf{q}_G^i\}_{i=1}^K$, Neural CDF barrier $\hat{h}(\mathbf{q}, t)$, safety margin η , Max. no. of bubbles N_{\max} , Min. radius r_{\min} .

Ensure: Graph \mathcal{G} containing bubbles from start to goals

```
1: function BUILDBUBBLEGRAPH( $\mathbf{q}_0, \{\mathbf{q}_G^i\}$ )
2:    $\mathcal{G}.V \leftarrow \{\mathcal{B}(\mathbf{q}_0, \hat{h}(\mathbf{q}_0, t) - \eta)\}, \quad \mathcal{G}.E \leftarrow \emptyset$ 
3:   while  $|\mathcal{G}.V| < N_{\max}$  do
4:      $\mathbf{q}_{\text{rand}} \leftarrow \text{SAMPLERANDOM}()$   $\triangleright$  With goal bias
5:      $\mathcal{B}_{\text{near}} \leftarrow \text{NEARESTBUBBLE}(\mathcal{G}, \mathbf{q}_{\text{rand}})$ 
6:     if  $\mathbf{q}_{\text{rand}}$  outside  $\mathcal{B}_{\text{near}}$  then
7:        $\mathbf{q}_{\text{new}} \leftarrow \text{EXTENDTOWARD}(\mathcal{B}_{\text{near}}, \mathbf{q}_{\text{rand}})$ 
8:        $r_{\text{new}} \leftarrow \hat{h}(\mathbf{q}_{\text{new}}, t) - \eta$ 
9:       if  $r_{\text{new}} > r_{\min}$  then
10:         $\mathcal{B}_{\text{new}} \leftarrow \mathcal{B}(\mathbf{q}_{\text{new}}, r_{\text{new}})$ 
11:         $\text{UPDATECONNECTIONS}(\mathcal{G}, \mathcal{B}_{\text{new}})$ 
12:   return  $\mathcal{G}$ 
13: function UPDATECONNECTIONS( $\mathcal{G}, \mathcal{B}_{\text{new}}$ )
14:   for  $\mathcal{B}_i \in \mathcal{G}.V$  do
15:     if  $\|\mathcal{B}_{\text{new}} \cdot \mathbf{q} - \mathcal{B}_i \cdot \mathbf{q}\| \leq r(\mathbf{q}_{\text{new}}) + r(\mathbf{q}_i)$  then
16:        $\mathcal{G}.E \leftarrow \mathcal{G}.E \cup (\mathcal{B}_{\text{new}}, \mathcal{B}_i)$ 
17:    $\mathcal{G}.V \leftarrow \mathcal{G}.V \cup \{\mathcal{B}_{\text{new}}\}$ 
```

This process continues until the maximum number of bubbles N_{\max} is reached or feasible paths to one goal configuration are identified.

B. Path Selection and Trajectory Optimization

Once the bubble-based graph \mathcal{G} is constructed, we must extract and refine a collision-free path connecting the start configuration \mathbf{q}_0 to one of the K goal configurations $\{\mathbf{q}_G^i\}$. Since \mathcal{G} may contain multiple feasible routes, we first select an optimal path according to a desired criterion (e.g., minimum total edge distance). We then solve a local trajectory optimization problem, fitting a continuous curve through the sequence of bubbles to ensure a smooth, dynamically feasible trajectory that remains collision-free.

Path Selection. We assign a cost to each edge in \mathcal{G} , for instance, the single-sided Hausdorff distance between two overlapping bubbles [28]. A shortest-path search (e.g., Dijkstra [12] or A* [18]) is run from the start bubble to every goal bubble. The path with the lowest overall cost is then passed to the optimization step, as summarized in Algorithm 2.

Trajectory Optimization. To obtain a smooth trajectory, we optimize a sequence of Bézier curves connecting the start configuration \mathbf{q}_0 to the selected goal configuration \mathbf{q}_G^* through the path of bubbles $\{\mathcal{B}_1, \dots, \mathcal{B}_n\}$. Each Bézier curve segment of degree d is defined by its control points:

$$\gamma_j(t) = \sum_{l=0}^d \binom{d}{l} t^l (1-t)^{d-l} \mathbf{c}_{j,l}, \quad (15)$$

where $\mathbf{c}_{j,l} \in \mathbb{R}^m$ is the l -th control point of the j -th curve segment. The k -th derivative of a Bézier curve is also a Bézier curve, and its squared norm integral can be expressed as:

$$\int_0^1 \|\gamma_j^{(k)}(t)\|^2 dt = \mathbf{c}_j^\top \mathbf{Q}_k \mathbf{c}_j, \quad (16)$$

Algorithm 2 Path Selection and Trajectory Optimization

Require:

- 1: Graph \mathcal{G} with start bubble $\mathcal{B}_{\text{start}}$, goal bubbles $\{\mathcal{B}_{\text{goal}}^i\}_i$
- 2: Edge cost function $\text{EDGECOST}(\mathcal{B}_i, \mathcal{B}_j)$
- 3: Weights $\{w_k\}$ for trajectory cost

Ensure: Smooth collision-free Bézier trajectory from \mathbf{q}_0 to some \mathbf{q}_G^i

```
4: function PATHSELECTANDOPTIMIZE( $\mathcal{G}, \mathcal{B}_{\text{start}}, \{\mathcal{B}_{\text{goal}}^i\}$ )
5:    $\text{bestCost} \leftarrow \infty, \quad \text{bestPath} \leftarrow \text{None}, \quad i_{\text{best}} \leftarrow -1$ 
6:   for  $i = 1 \rightarrow K$  do
7:      $\text{path}_i \leftarrow \text{SHORTESTPATH}(\mathcal{G}, \mathcal{B}_{\text{start}}, \mathcal{B}_{\text{goal}}^i, \text{EDGECOST})$ 
8:     if  $\text{path}_i$  exists then
9:        $\text{cost}_i \leftarrow \text{PATHCOST}(\text{path}_i, \text{EDGECOST})$ 
10:      if  $\text{cost}_i < \text{bestCost}$  then
11:         $\text{bestCost} \leftarrow \text{cost}_i, \text{bestPath} \leftarrow \text{path}_i, i_{\text{best}} \leftarrow i$ 
12:   if  $\text{bestPath} = \text{None}$  then
13:     return failure  $\triangleright$  No feasible path found
14:    $\text{curves} \leftarrow \text{BEZIEROPT1}(\text{bestPath}, \{w_k\})$   $\triangleright$  Eq. (17)
15:   return ( $\text{curves}, i_{\text{best}}$ )
```

where \mathbf{c}_j is the vectorized form of all control points in segment j , and \mathbf{Q}_k is a positive semidefinite matrix. This leads to the following convex quadratically constrained quadratic program:

$$\begin{aligned} \min_{\{\mathbf{c}_{j,i}\}} \quad & \sum_{j=1}^n \sum_{k=1}^K w_k \int_0^1 \|\gamma_j^{(k)}(t)\|^2 dt \\ \text{subject to} \quad & \|\mathbf{c}_{j,l} - \mathbf{q}_j\|^2 \leq r(\mathbf{q}_j)^2, \quad \forall j, l \\ & \gamma_j(1) = \gamma_{j+1}(0), \quad j = 1, \dots, n-1 \\ & \gamma_j^{(k)}(1) = \gamma_{j+1}^{(k)}(0), \quad j = 1, \dots, n-1, k = 1, 2 \\ & \gamma_1(0) = \mathbf{q}_0, \quad \gamma_n(1) = \mathbf{q}_G^*, \\ & \gamma_1^{(i)}(0) = \mathbf{0}, \quad \gamma_n^{(i)}(1) = \mathbf{0}, \quad i = 1, \dots, d \end{aligned} \quad (17)$$

where $\mathbf{c}_{j,i}$ are the control points of the j -th Bézier curve segment γ_j of degree d , and $\gamma_j^{(k)}$ denotes its k -th derivative. The objective minimizes a weighted sum of integrated squared derivatives, promoting smoothness. The first constraint ensures safety by keeping control points within their respective bubbles, which by the convex hull property of Bézier curves guarantees the entire trajectory remains collision-free. The remaining constraints enforce continuity of position and derivatives between segments, as well as boundary conditions including zero velocity at endpoints. Unlike traditional sampling-based planners that may not have safety guarantees or require additional collision checks for post-optimized trajectory, our formulation provides a convex optimization problem that simultaneously guarantees smoothness and safety without requiring additional collision checking.

Throughout this section, we have introduced the **bubble-CDF planner**, which leverages neural CDF barriers to efficiently explore the configuration space while ensuring safety. By constructing *configuration-space bubbles* around safe configurations and dynamically adjusting step sizes based on bubble radii, our approach significantly reduces collision-checking overhead. Additionally, the trajectory optimization formulation in (17) guarantees smooth, dynamically feasible paths without requiring post-processing for collision checks.

Thus far, we have focused on global planning in static environments, assuming a time-invariant and accurate neural CDF barrier $\hat{h}(\mathbf{q}, t)$. However, real-world deployments must contend with dynamic obstacles, CDF modeling errors, and sensor uncertainties. In Section VI, we introduce a distributionally robust control formulation to track the planned path in real time, explicitly accounting for these uncertainties to ensure safe and adaptive execution.

VI. DISTRIBUTIONALLY ROBUST MANIPULATION CONTROL

In this section, we present a control synthesis approach that guarantees safe real-time configuration trajectory tracking using imperfect neural CDF barrier estimates (due to sensing and modeling errors) even in the presence of dynamic obstacles. We first describe our approach to track the reference trajectory (Sec. VI-A). We then incorporate a distributionally robust control barrier function (DR-CBF) [34] to ensure safe control synthesis despite dynamic obstacles and neural CDF barrier uncertainty (Sec. VI-B).

A. Governor-based Trajectory Tracking

We first present our approach for tracking the planned piecewise Bézier configuration trajectory $\gamma : [0, 1] \rightarrow \mathcal{Q}$, obtained in Sec. V-B, in the absence of safety constraints. Inspired by Garone and Nicotra [16], Li et al. [31], we design a reference governor to determine a dynamically changing reference configuration $\gamma(s)$ along the trajectory, where $s \in [0, 1]$ is a progress variable. In other word, $\gamma(0) = \mathbf{q}_0$ is the initial robot configuration, while $\gamma(1) = \mathbf{q}_G$ is one of the goal configurations. The governor system adapts the value of the progress variable s based on the manipulator's current configuration to ensure smooth progress along the trajectory. We then stabilize the manipulator configuration \mathbf{q} to $\gamma(s)$ using a proportional-derivative (PD) controller.

The dynamics of s are designed to balance the robot's tracking capabilities with smooth progression along the trajectory:

$$\dot{s} = \frac{k}{1 + \|\mathbf{q} - \gamma(s)\|} (1 - s^\zeta), \quad (18)$$

where $k > 0$ is a gain parameter, $\zeta \geq 1$ controls the rate of saturation as s approaches 1, and $\|\mathbf{q} - \gamma(s)\|$ is the Euclidean distance between the current and reference configuration. This adaptive mechanism accelerates s when the manipulator is near the reference and decelerates it when farther away, ensuring smooth progression without abrupt jumps.

To have the manipulator track the reference trajectory γ , we employ a PD controller as the nominal controller, which stabilizes the manipulator to the current local goal $\gamma(s)$:

$$\bar{\mathbf{u}}(\mathbf{q}, t) = -K_P(\mathbf{q} - \gamma(s)) - K_D\dot{\mathbf{q}}, \quad (19)$$

where K_P and K_D are positive definite matrices controlling the proportional and derivative contributions, respectively. The first term ensures that the robot is drawn towards $\gamma(s)$, while the second term provides damping to minimize oscillations.

B. Distributionally Robust Neural CDF Barrier

To ensure safe operation while tracking the planned trajectory, the robot's configuration \mathbf{q} must remain within the safe set $\mathcal{C}_{\text{safe}}(t)$ as defined in (10). We utilize the CDF barrier as control barrier functions (CBFs) [3] by considering its time derivative. This leads to the following time-varying control barrier condition (CBC),

$$\begin{aligned} \text{CBC}(\mathbf{q}, \mathbf{u}, t) &:= \nabla_{\mathbf{q}} h(\mathbf{q}, t)^\top \mathbf{u} + \frac{\partial h(\mathbf{q}, t)}{\partial t} + \alpha_h(h(\mathbf{q}, t)) \quad (20) \\ &= \underbrace{[\nabla_{\mathbf{q}} h(\mathbf{q}, t)^\top, \alpha_h(h(\mathbf{q}, t)), \frac{\partial h(\mathbf{q}, t)}{\partial t}]^\top}_{\boldsymbol{\xi}^\top(\mathbf{q}, t)} \begin{bmatrix} \mathbf{u} \\ 1 \\ 1 \end{bmatrix}, \end{aligned}$$

where α_h is a class \mathcal{K}_∞ function.

With the nominal PD control law $\bar{\mathbf{u}}(\mathbf{q}, t)$ in (19), one can enforce safety by solving CBF quadratic program (QP) [2] that generates the safe manipulator velocity control:

$$\begin{aligned} \mathbf{u}^* &= \arg \min_{\mathbf{u} \in \mathcal{U}} \|\mathbf{u} - \bar{\mathbf{u}}(\mathbf{q}, t)\|^2 \\ \text{s.t. } &\text{CBC}(\mathbf{q}, \mathbf{u}, t) \geq 0, \end{aligned} \quad (21)$$

where $\mathcal{U} := \{\mathbf{u}_{\min} \leq \mathbf{u} \leq \mathbf{u}_{\max}\}$ defines the admissible control space, ensuring the commanded manipulator velocities remain within feasible operational limits. However, the CDF barrier $h(\mathbf{q}, t)$ and its gradients are not known exactly but rather are approximated through the neural CDF barrier $\hat{h}(\mathbf{q}, t)$ in (12). Due to uncertainties introduced by the neural network model and the point-cloud data, \hat{h} cannot be treated as an exact representation of h . Instead, we work with samples of the associated uncertainty vector $\{\boldsymbol{\xi}_i\}_{i \in [N]}$, defined in (20), which capture the variations in \hat{h} , its gradient, and its time derivative. The practical approach of obtaining such samples is discussed in Sec. VI-C.

Drawing inspiration from recent advances in distributionally robust optimization (DRO) [14, 34], we reformulate the CBC in a distributionally robust manner:

$$\inf_{\mathbb{P} \in \mathcal{M}_N^r} \mathbb{P}(\text{CBC}(\mathbf{q}, \mathbf{u}, \boldsymbol{\xi}) \geq 0) \geq 1 - \epsilon, \quad (22)$$

where \mathcal{M}_N^r is a Wasserstein ambiguity set constructed from $\{\boldsymbol{\xi}_i\}_{i=1}^N$ and ϵ is a user-specified risk tolerance. To formally define \mathcal{M}_N^r , let $\Xi \subseteq \mathbb{R}^{m+2}$ denote the space of uncertainty vectors $\boldsymbol{\xi}$, and let $\mathcal{P}_p(\Xi)$ be the space of all Borel probability measures over Ξ with finite p -th moment, by utilizing the p -Wasserstein distance W_p [14], the ambiguity set

$$\mathcal{M}_N^r := \{\mu \in \mathcal{P}_p(\Xi) \mid W_p(\mu, \mathbb{P}_N) \leq r\} \quad (23)$$

defines a ball of distributions around the discrete empirical distribution $\mathbb{P}_N := \frac{1}{N} \sum_{i=1}^N \delta_{\boldsymbol{\xi}_i}$ of the samples.

This DRO formulation provides probabilistic safety guarantees by ensuring the safety constraint holds with high probability for all distributions around \mathbb{P}_N . The Wasserstein ambiguity set measures the distribution similarity and its parameters (radius r and risk tolerance ϵ) offer flexibility to account for different levels of uncertainty due to sensor noise

and neural model inaccuracies, without requiring explicit or precise knowledge of the true distribution of ξ .

Next, by utilizing the 1-Wasserstein distance and following a convex reformulation of the DR-CBF in [34, Proposition 6.5], lead to the following optimization problem, whose feasibility implies the DRO constraint in (22):

$$\begin{aligned} \mathbf{u}^* = & \arg \min_{\mathbf{u} \in \mathcal{U}, s \in \mathbb{R}, \beta_i \in \mathbb{R}} \|\mathbf{u} - \bar{\mathbf{u}}(\mathbf{q}, t)\|^2, \\ \text{s.t. } & r\|\mathbf{u}\|_\infty \leq s\epsilon - \frac{1}{N} \sum_{i=1}^N \beta_i, \\ & \beta_i \geq \max\{s - [\mathbf{u} \ 1 \ 1]^\top \xi_i(\mathbf{q}, t), 0\}, \forall i \in [N]. \end{aligned} \quad (24)$$

The reformulation maintains the linear dependence of the constraints on \mathbf{u} , ensuring that the optimization remains a QP and can be solved efficiently in real time. By integrating the DR-CBF constraint into the control synthesis, the proposed DR-CBF-QP safety filter enables robust and safe operation in dynamic environments.

C. Uncertainty Sample Selection

This section details our approach for obtaining samples $\{\xi_i\}_{i=1}^N$ of the uncertainty vector ξ in the CBC in (20).

The definition of the neural CDF barrier $\hat{h}(\mathbf{q}, t)$ in (12) depends on the point-cloud data $\mathcal{P}(t)$. The point cloud is represented as $\mathcal{P}(t) = \{\mathbf{p}_j\}_{j=1}^{M_1}$, where each $\mathbf{p}_j \in \mathbb{R}^3$ corresponds to a workspace point captured at time t . The velocity of each point, denoted as $\frac{\partial \mathbf{p}_j}{\partial t}$, is also considered to account for dynamics in the environment.

To account for uncertainty in the neural CDF model $\hat{f}(\mathbf{p}, \mathbf{q})$, we employ Monte Carlo (MC) dropout in the network architecture [15]. This allows us to perform M_2 stochastic forward passes through the robot CDF neural network, collecting multiple realizations of $\hat{f}_c(\mathbf{p}, \mathbf{q}; \theta)$, along with its gradients. Specifically, for each forward pass of $f_c^{(i)}$, we evaluate $f_c^{(i)}$ across all M_1 points in $\mathcal{P}(t)$. Consequently, we obtain $M_1 \times M_2$ realizations of:

$$\left\{ f_c^{(i)}(\mathbf{p}_j, \mathbf{q}), \nabla_{\mathbf{q}} f_c^{(i)}(\mathbf{p}_j, \mathbf{q}), \nabla_{\mathbf{p}} f_c^{(i)}(\mathbf{p}, \mathbf{q})^\top \frac{\partial \mathbf{p}_j}{\partial t} \right\}, \quad (25)$$

where $i \in [M_2]$ corresponds to the MC dropout realization and $j \in [M_1]$ corresponds to the point in $\mathcal{P}(t)$.

From the $M_1 \times M_2$ realizations, we select $N \ll M_1 \times M_2$ samples in the set (25) based on the N minimal values of

$$\alpha_h(f_c^{(i)}(\mathbf{p}_j, \mathbf{q})) + \nabla_{\mathbf{p}} f_c^{(i)}(\mathbf{p}, \mathbf{q})^\top \frac{\partial \mathbf{p}_j}{\partial t}, \quad (26)$$

which effectively identifies samples $\{\xi_i\}_{i \in [N]}$.

In this section, we introduced a DR-CBF control formulation that ensures safe manipulation under uncertainty. Unlike naive safety margin adjustments, our approach explicitly accounts for uncertainties in the neural CDF model, its gradient estimates, and point-cloud velocity observations. By leveraging a Wasserstein ambiguity set, we optimize for the worst-case uncertainty within a data-driven confidence region, providing stronger safety guarantees than standard

CBF formulations. This enables adaptive and robust control in dynamic environments without requiring explicit probabilistic models of uncertainty.

VII. EVALUATION

This section evaluates our planning and control techniques, which utilize neural CDF barriers, in simulations on 2-DoF planar arm and 6-DoF xArm as well as in real-world experiments on 6-DoF xArm. We evaluate the computational efficiency and solution quality of the bubble-CDF planner and the robustness of the DR-CBF controller in ensuring safety under dynamic obstacles and uncertainty.

A. Implementation Details

Training Dataset and Loss Function: We discretize the robot's workspace into a $40 \times 40 \times 40$ grid. For each workspace point, we generate contact configurations using BFGS optimization, and then select 200 diverse configurations via farthest-point sampling in configuration space [29]. During training, we employ an online batching strategy where each batch randomly samples 10 configurations and 50 workspace points. For each configuration-point pair $(\mathbf{p}_i, \mathbf{q}_i)$, the ground-truth environment CDF value $f_c^*(\mathbf{p}_i, \mathbf{q}_i)$ is computed as the minimum joint-space distance to the set of contact configurations associated with \mathbf{p}_i .

The network is trained using the following loss function:

$$\begin{aligned} \mathcal{L}_{\text{env}} = & \frac{1}{N_1 N_2} \sum_{i=1}^{N_1} \sum_{j=1}^{N_2} \left(\hat{f}_c(\mathbf{p}_i, \mathbf{q}_j; \theta_1) - f_c^*(\mathbf{p}_i, \mathbf{q}_j) \right)^2 \\ & + \lambda \left(\|\nabla_{\mathbf{q}} \hat{f}_c(\mathbf{p}_i, \mathbf{q}_j; \theta_1)\| - 1 \right)^2, \end{aligned} \quad (27)$$

where $\lambda = 0.05$ is a user-specified weight.

For the self-collision CDF (SCDF), we generate training data by uniformly sampling joint configurations and detecting self-collisions using the PyBullet simulation engine [8]. Each self-colliding configuration $\mathbf{q}' \in \mathcal{C}_{\text{sc}}$ is stored along with the minimal joint index range $[a : b]$ responsible for the collision. During training, each batch consists of N randomly sampled configurations $\{\mathbf{q}_j\}_{j=1}^N$. For each configuration, the ground-truth SCDF value $f_{\text{sc}}^*(\mathbf{q}_j)$ is computed according (8).

The SCDF network is trained with the following loss:

$$\begin{aligned} \mathcal{L}_{\text{sc}} = & \frac{1}{N_3} \sum_{j=1}^{N_3} \left(\hat{f}_{\text{sc}}(\mathbf{q}_j; \theta_2) - f_{\text{sc}}^*(\mathbf{q}_j) \right)^2 \\ & + \lambda \left(\|\nabla_{\mathbf{q}} \hat{f}_{\text{sc}}(\mathbf{q}_j; \theta_2)\| - 1 \right)^2, \end{aligned} \quad (28)$$

where $\lambda = 0.05$ is user-specified weight.

Network Architecture and Training Setup: The neural CDF and SCDF are each implemented as a 5-layer fully connected multilayer perceptron (MLP) with GELU activation functions [21]. Skip connections are included at the second and fourth layers to improve learning stability. Both networks are trained using PyTorch on an NVIDIA RTX 4090 GPU for

TABLE I: Inference time (ms) of Neural CDF barrier on xArm for varying batch sizes of configurations (\mathbf{q}) and workspace points (\mathbf{p}).

$\mathbf{q} \backslash \mathbf{p}$	1	10	100	1000	10000
1	0.272	0.281	0.295	0.291	0.742
10	0.281	0.307	0.297	0.758	6.818
100	0.301	0.301	0.763	7.060	70.215

50,000 epochs with the Adam optimizer and a learning rate of 2×10^{-4} .

Training Results: The environment CDF model is evaluated on a held-out test set consisting of 50,000 triplets of configurations (\mathbf{q}), workspace points (\mathbf{p}), and corresponding CDF values. It achieves a Mean Absolute Error (MAE) of 0.041 radians and a Root Mean Square Error (RMSE) of 0.073 radians. Similarly, the SCDF model is evaluated on 10,000 held-out configurations with known self-collision distances, achieving MAE of 0.029 radians and RMSE of 0.054 radians. As shown in Table I, the combined inference time for evaluating both the environment CDF and the self-collision CDF, which together define the neural CDF barrier in (12), remains efficient across different batch sizes. This scalability allows the framework to be effectively integrated with sampling-based motion planning algorithms and real-time control using point cloud observations.

B. Baselines and Parameters

We compare our approach against the following baselines.

- **Planners:**

- CDF-RRT: RRT with collision checks based on the neural CDF barrier.
- SDF-RRT [47]: RRT with collision checks using a neural SDF barrier.
- SDF-RRT-Connect [26]: A variant of SDF-RRT with a bi-directional search strategy.
- SDF-Lazy-RRT [19]: A variant of SDF-RRT with reduced collision-checking overhead.

- **Controllers:**

- PD Controller: A proportional-derivative controller $\bar{\mathbf{u}}(\mathbf{q}, t)$ focused solely on trajectory tracking.
- PD + CBF-QP [7]: A PD controller $\bar{\mathbf{u}}(\mathbf{q}, t)$ augmented with a CBF-QP safety filter, where the CBF is constructed using the neural CDF barrier. However, this approach disregards uncertainty in the CDF model or sensor measurements, unlike ours.

The baseline planners are implemented using the Open Motion Planning Library (OMPL) [41], ensuring consistency across all algorithms. All controllers are implemented using Casadi [4], and the CBF-QP and our DR-CBF-QP problems are solved using the interior point optimizer, operating at a control frequency of 50 Hz.

Evaluation Metrics: For planners, we evaluate the number of collision checks and path length. For controllers, the evaluation metrics include success rate (percentage of trials where the robot safely reaches the goal) and tracking error (measured as the Fréchet distance between planned and executed paths).

TABLE II: Planner parameters used for evaluation. **Goal bias** specifies the probability of sampling configurations directly toward the goal. **Step size** defines the maximum extension distance during tree expansion. **Safety margin** indicates the minimum clearance required for collision checking, and **collision check resolution** determines the granularity of edge validity checks, expressed as a fraction of the configuration space diagonal. For the 2-DoF planar robot, a resolution of 0.01 corresponds to 0.089 radians, while for the 6-DoF xArm, a resolution of 0.002 corresponds to 0.04 radians.

Planner	Goal Bias	Step Size	Safety Margin	Col. Check Resolution
Baselines	0.1	0.1	0.05	0.01 (2-DoF) / 0.002 (6-DoF)
Bubble-CDF	0.1	N/A	0.05	N/A

Parameters: Tables II and III summarize the parameters used for the planners and controllers.

TABLE III: Control parameters used for evaluation. The PD control gains K_P and K_D are positive definite matrices, assumed to be diagonal with identical values along the diagonal. The function α_h is a linear class \mathcal{K}_∞ function used in the CBF formulation. Parameters k and ζ define the governor dynamics in (18). The risk tolerance ϵ and sample size N correspond to the DR-CBF in (22), while r represents the Wasserstein radius.

Parameter	K_P	K_D	α_h	k	ζ	ϵ	N	r
Value	0.8	0.1	1.0	0.2	12	0.1	10	0.02

C. 2-DoF Planar Robot Simulation

We begin by evaluating our bubble-CDF planner against baseline sampling-based global motion planning approaches on a 2-DoF planar robotic arm. The arm consists of two links, each 2 meters long, with a fixed base located at the origin (0, 0). The joint angles are constrained within the range $[-\pi, \pi)$, and the initial configuration is set to (0, 0), placing the end-effector at (4, 0), as illustrated in Fig. 1.

Setup: We assess the performance of the bubble-CDF planner and all baselines in 500 randomly generated environments. Each environment includes 4 static obstacles of varying sizes and positions, and the end-effector goal is randomly sampled to be at least 4 meters away from its initial position while ensuring reachability. The robot receives point-cloud observations of the obstacle surfaces. Due to the 2-DoF planar structure, most reachable end-effector positions correspond to two distinct goal configurations, and the planners are tasked with finding a feasible path from the initial configuration to either one of the two goal configurations.

Results and Discussion: Table IV summarizes the performance metrics across all 500 environments. All planners succeed in finding the path. The results demonstrate the significant efficiency of the bubble-CDF planner in reducing the number of collision checks, reducing the planning time, while maintaining comparable path quality. The bubble-CDF planner requires 153.8 ± 62.2 collision checks, while even the best baseline (Lazy-RRT) requires at least $10\times$ more collision checks. As a result, bubble-CDF achieves the lowest planning time of all methods at 0.17 ± 0.05 seconds. This showcases the ability of our proposed bubble-CDF planner to explore the configuration space more efficiently. Despite this reduction, the bubble-based planner produces paths with similar lengths (3.72 ± 0.81) radians to those of the baselines.

Next, we present our evaluation of the proposed DR-CBF-QP formulation for safe control synthesis on a planar robot.

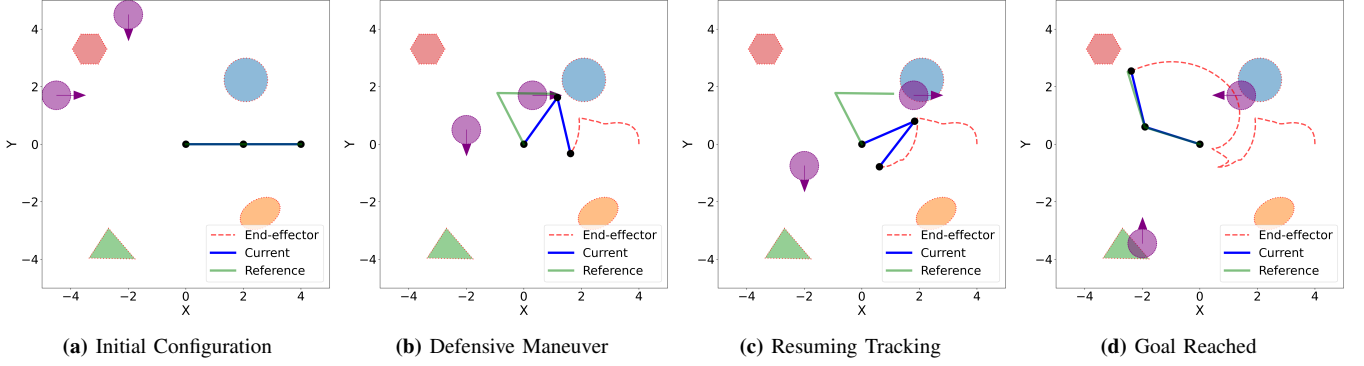


Fig. 2: Snapshots of a 2-link arm navigating a dynamic environment with purple obstacles (velocity directions shown by arrows). The arm is tasked to follow the planned path in Fig. 1. The arm is shown in blue and the trajectory of its end-effector is shown in red, and the local reference configuration goal $\gamma(s)$ is shown in green.

TABLE IV: Planning performance comparison on a 2-DoF planar robot.

Planner	Col. Checks	Path Length	Time (s)
CDF-RRT	2108.9 \pm 438.7	3.64 \pm 0.69	0.33 \pm 0.06
SDF-RRT [47]	2118.3 \pm 388.9	3.61 \pm 0.69	0.29 \pm 0.04
SDF-RRT-Connect	2144.6 \pm 459.7	3.63 \pm 0.74	0.33 \pm 0.05
SDF-Lazy-RRT	1759.2 \pm 299.3	3.75 \pm 0.83	0.31 \pm 0.06
Bubble-CDF	153.8 \pm 62.2	3.72 \pm 0.81	0.13 \pm 0.04

TABLE V: Control performance comparison on a 2-DoF planar robot.

Controller	Static		Dynamic	
	Success Rate	Tra. Error	Success Rate	Tra. Error
PD	0.874	0.068 \pm 0.017	0.112	0.062 \pm 0.027
PD + CBF-QP [7]	0.982	0.131 \pm 0.049	0.638	0.217 \pm 0.106
PD + DR-CBF-QP	1.0	0.173 \pm 0.074	0.992	0.394 \pm 0.172

Setup: The controllers are evaluated in both static (Fig. 1) and dynamic environments (Fig. 2). In both settings, point cloud data of the obstacle surfaces is provided to the robot. For dynamic environments, obstacle velocities are sampled from a normal distribution, $v \sim \mathcal{N}(0.5, 0.1)$ m/s, while the robot is provided with a nominal velocity of $v = 0.5$ m/s for control synthesis. Each controller is evaluated for 500 random trials in both static and dynamic environments.

In both scenarios, the objective is to track the bubble-CDF planned trajectory γ (Fig. 1) while avoiding collisions.

Results and Discussion: Table V presents the control performance across static and dynamic environments. The proposed DR-CBF-QP formulation achieves a 100% success rate in static environments and high success rate (99.2%) in dynamic environments, outperforming both the PD controller and the standard CBF-QP approach. The PD controller, designed solely for trajectory tracking without obstacle avoidance, exhibits the lowest success rates in both static and dynamic environments. The baseline CBF-QP shows good performance in static scenarios, but its success rate significantly deteriorates in dynamic environments (63.8%). We attribute this degradation to disregarding uncertainties in dynamic obstacle velocities.

While the DR-CBF-QP formulation demonstrates higher tracking errors compared to the baselines, this trade-off reflects its emphasis on maintaining safety. The method adjusts the robot's trajectory to prioritize collision avoidance, especially in dynamic environments where safety margins must adapt to

TABLE VI: Planning performance comparison on a 6-DoF xArm robot in Pybullet Simulation.

Planner	Col. Checks	Path Length	Time (s)
CDF-RRT	3415.4 \pm 803.6	3.11 \pm 0.46	0.75 \pm 0.23
SDF-RRT [47]	3251.8 \pm 782.4	3.07 \pm 0.49	0.73 \pm 0.20
SDF-RRT-Connect	3437.4 \pm 723.2	3.11 \pm 0.43	0.71 \pm 0.21
SDF-Lazy-RRT	2741.1 \pm 737.9	3.15 \pm 0.53	0.72 \pm 0.22
Bubble-CDF	278.5 \pm 80.7	3.04 \pm 0.46	0.15 \pm 0.06

uncertainties in obstacle motion and CDF estimates.

Qualitatively, the defensive maneuvers and adaptability of the DR-CBF-QP formulation are evident in Fig. 2. In dynamic environments, the robot effectively adjusts its trajectory to avoid collisions, as shown in Fig. 2b, where it performs a defensive maneuver to bypass a moving obstacle. Subsequently, it resumes tracking the planned trajectory (Fig. 2c) and successfully reaches the goal configuration (Fig. 2d).

D. 6-DoF xArm Robot Simulation

Next, we present simulated experiments for a 6-DoF xArm robotic manipulator in Pybullet [8] with static and dynamic obstacles to further evaluate our proposed approach.

Setup: The simulation environment consists of a 6-DoF xArm robot positioned on a table next to a shelf, as illustrated in Fig. 3. A depth camera provides point-cloud observations of the obstacles. We conducted 50 randomized trials by varying the shelf position and selecting different random goal positions. For each trial, inverse kinematics was used to determine five feasible goal configurations, and motion planning was performed in a static environment using these configurations.

To evaluate controller performance, the best planned path from the bubble-CDF planner was selected for tracking in each trial. Additionally, three dynamic obstacles were introduced into the scene, with their positions and velocities varying but assumed to be known to the robot. The velocities of the dynamic obstacles were sampled from a normal distribution, $v \sim \mathcal{N}(0.2, 0.05)$ m/s.

Results and Discussion: Table VI summarizes the planning results for the 6-DoF xArm robot. Similar to the 2-DoF case, the bubble-CDF planner significantly outperforms baseline methods in terms of collision checks and planning time.

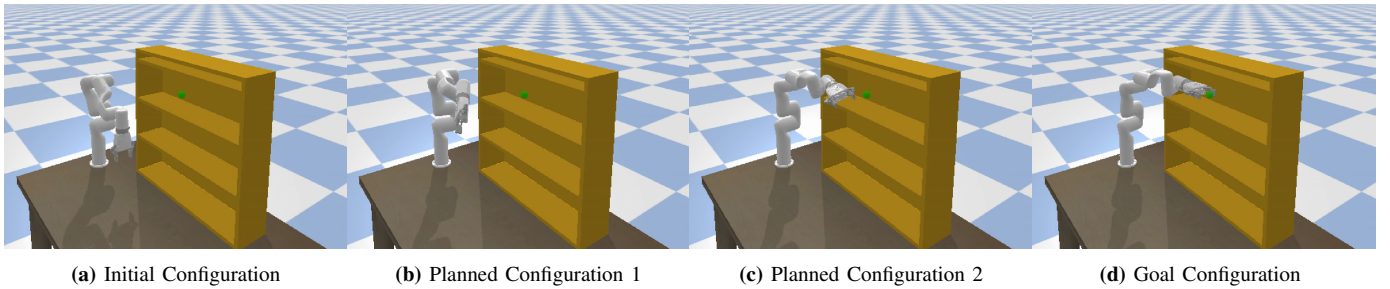


Fig. 3: Bubble-CDF planning for a 6-DoF xArm robot in a static environment, targeting an end-effector goal represented by a green sphere. (a) The initial configuration of the xArm. (b, c) Intermediate configurations illustrating the planned path as the robot avoids obstacles while progressing toward the goal. (d) The final goal configuration reached by the robot.

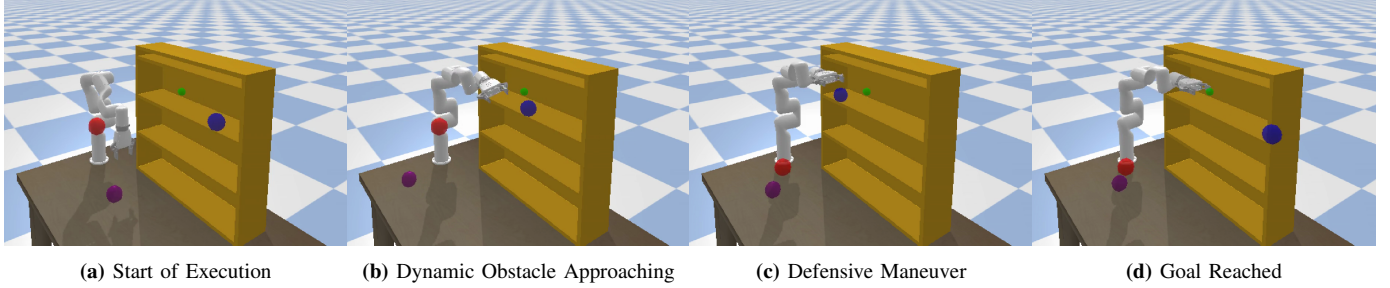


Fig. 4: Snapshots of safe control execution on a 6-DoF xArm robot in an environment with dynamic obstacles. (a) The control execution begins at the initial configuration. (b) A dynamic obstacle (blue) approaches the robot from right. (c) The robot executes a defensive maneuver, moving upward to avoid the obstacle. (d) The robot successfully resumes tracking and reaches the goal configuration.

Path lengths across all planners remain comparable, indicating that the bubble-CDF approach does not compromise solution quality.

Figure 3 illustrates the planned path generated by the bubble-CDF planner in a static environment for a specific end-effector goal inside the shelf. Among the five possible goal configurations derived from inverse kinematics, the planner selects the shortest collision-free path.

Table VII quantitatively compares the control performance of different controllers under both static and dynamic environments. The baseline PD controller achieves a success rate of 68% in the static environment but struggles significantly in dynamic scenarios, with a success rate dropping to 18%, highlighting its inability to effectively react to moving obstacles.

The addition of a CBF-QP safety filter improves the success rate to 88% in static environments. However, in dynamic scenarios, its success rate remains limited at 70%, suggesting that while CBF constraints enhance obstacle avoidance, they do not account for errors in CDF modeling and point-cloud observations. In contrast, our proposed PD + DR-CBF-QP achieves a 100% success rate in both static and dynamic environments, demonstrating its robustness against dynamic obstacles and uncertainty. The increased tracking error reflects the adaptive nature of our approach, which prioritizes safety by dynamically adjusting the trajectory to avoid obstacles, even if it deviates from the originally planned path.

Figure 4 illustrates the execution of a planned path by the 6-DoF xArm robot in a dynamic environment. The robot begins at the initial configuration (Fig. 4a) and dynamically reacts to an approaching obstacle (blue) as shown in Fig. 4b. By executing a defensive maneuver (Fig. 4c), the robot moves

TABLE VII: Control performance comparison on a 6-DoF xArm robot in Pybullet Simulation.

Controller	Static		Dynamic	
	Success Rate	Tra. Error	Success Rate	Tra. Error
PD	0.68	0.053 ± 0.014	0.18	0.051 ± 0.013
PD + CBF-QP [7]	0.88	0.115 ± 0.046	0.70	0.327 ± 0.104
PD + DR-CBF-QP	1.0	0.143 ± 0.055	1.0	0.516 ± 0.221

TABLE VIII: Planning performance comparison on a real 6-DoF xArm robot.

Planner	Col. Checks	Path Length	Time (s)
CDF-RRT	5617.4 ± 1333.6	3.71 ± 0.71	1.02 ± 0.33
SDF-RRT [47]	5911.9 ± 1487.7	3.72 ± 0.68	1.04 ± 0.33
SDF-RRT-Connect	5801.5 ± 1265.4	3.75 ± 0.63	1.05 ± 0.36
SDF-Lazy-RRT	4765.8 ± 1331.4	3.84 ± 0.69	0.96 ± 0.32
Bubble-CDF	634.8 ± 225.1	3.81 ± 0.66	0.22 ± 0.08

upward to maintain safety and avoid a collision. After the obstacle passes, the robot resumes trajectory tracking and successfully reaches the goal configuration (Fig. 4d).

E. 6-DoF xArm Robot Experiments

To further validate the efficiency of the bubble-CDF planner and the robustness of the DR-CBF controller, we conducted real-world experiments on a 6-DoF xArm manipulator in several cluttered and dynamic environments.

Setup: The experimental environment consists of a 6-DoF xArm robot operating on a table in a cluttered workspace with static obstacles, as shown in Fig. 5. A depth camera provides point-cloud observations of the scene. We conducted 20 randomized trials by varying obstacle placements and selecting different goal configurations. Planning was performed assuming the static environment. During execution, the robot followed the planned path while dynamic obstacles were introduced. The velocity of the moving objects is estimated using ArUco markers.

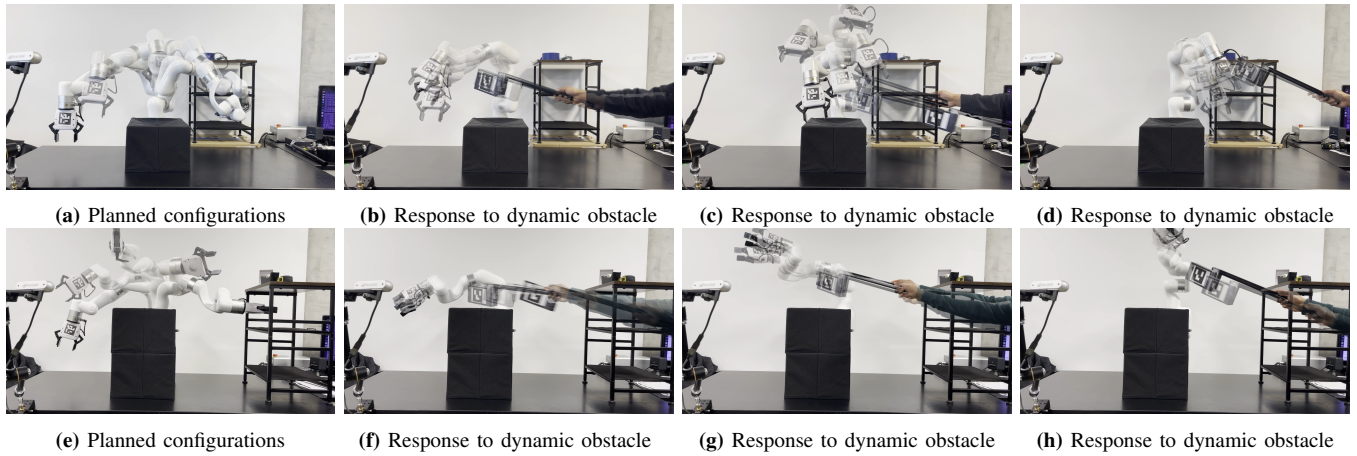


Fig. 5: Bubble-CDF planner and DR-CBF control applied to two real-world setups for a 6-DoF xArm robot. The top row (a-d) represents Setup 1, with the robot navigating a cluttered environment featuring a combination of static and dynamic obstacles. Similarly, the bottom row (e-h) depicts Setup 2, showcasing the planner’s adaptability in a different obstacle layout. For both setups: (a, e) illustrate the bubble-CDF planned configuration in static environments, while (b-d, f-h) demonstrate the robot’s real-time adaptive responses to dynamic obstacles.

Results and Discussion: Table VIII presents a quantitative comparison of planning performance across different methods. The proposed bubble-CDF planner achieves an order-of-magnitude reduction in the number of collision checks compared to all baseline methods and reduces the average planning time by a factor of five, decreasing from 1.0 seconds to about 0.2 seconds. This improvement stems from the use of configuration-space bubbles, which certify local collision-free regions and minimize the need for frequent edge-based collision checking. Consistent with simulation results, the generated path lengths remain comparable across all methods, demonstrating that our approach maintains solution quality while substantially improving efficiency.

Figure 5 shows snapshots of the bubble-CDF planner and DR-CBF controller in two different workspace arrangements. The robot exhibits similar behavior to the simulation, following the nominal planned trajectory (Figs. 5a, 5e) but stopping and avoiding dynamic obstacles as they are presented. Video recordings of these experiments are shown in the supplementary material.

VIII. CONCLUSION

In this work, we proposed an integrated framework for safe motion planning and control of robotic manipulators in dynamic and cluttered environments. Our approach combines a novel bubble-CDF planner for efficient trajectory generation and a distributionally robust control barrier function (DR-CBF) formulation for safe navigation. Comprehensive evaluations, conducted in both simulation and real-world settings, validate the effectiveness of our approach, demonstrating high success rates and significant reductions in computational overhead.

The bubble-CDF planner leverages the neural configuration-space distance function (CDF) to construct local safety regions, termed *configuration-space bubbles*, enabling efficient exploration of the configuration space. By certifying entire regions as collision-free with a single query, the planner significantly reduces the number of collision checks compared

to conventional sampling-based methods. This efficiency is achieved without compromising the quality of the planned trajectories, as evidenced by comparable path lengths to baseline approaches. Additionally, the planner allows trajectory optimization to be formulated as a convex program, enabling smooth and safe trajectory refinement without requiring additional collision checks.

For real-time trajectory execution, we introduced a DR-CBF-QP safety filter that ensures the robot remains within a safe set throughout its motion. This formulation explicitly incorporates uncertainties in the neural CDF model, gradient estimates, and sensor measurements, leveraging a distributionally robust optimization framework. The DR-CBF-QP controller dynamically adapts to obstacles and sensor inaccuracies, maintaining safety while ensuring smooth trajectory tracking in both static and dynamic environments.

REFERENCES

- [1] Adnan Ademovic and Bakir Lacevic. Path planning for robotic manipulators using expanded bubbles of free c-space. In *IEEE International Conference on Robotics and Automation (ICRA)*, pages 77–82, 2016. doi: 10.1109/ICRA.2016.7487118. 2
- [2] Aaron D Ames, Xiangru Xu, Jessy W Grizzle, and Paulo Tabuada. Control barrier function based quadratic programs for safety critical systems. *IEEE Transactions on Automatic Control*, 62(8):3861–3876, 2017. 6
- [3] Aaron D. Ames, Samuel Coogan, Magnus Egerstedt, Gennaro Notomista, Koushil Sreenath, and Paulo Tabuada. Control barrier functions: Theory and applications. In *2019 18th European Control Conference (ECC)*, pages 3420–3431, 2019. 6
- [4] Joel A E Andersson, Joris Gillis, Greg Horn, James B Rawlings, and Moritz Diehl. CasADi – A software framework for nonlinear optimization and optimal control. *Mathematical Programming Computation*, 11(1): 1–36, 2019. doi: 10.1007/s12532-018-0139-4. 8

- [5] Joshua Bialkowski, Michael Otte, Sertac Karaman, and Emilio Frazzoli. Efficient collision checking in sampling-based motion planning via safety certificates. *The International Journal of Robotics Research*, 35(7):767–796, 2016. 2
- [6] Oliver Brock and Lydia Kavraki. Decomposition-based motion planning: A framework for real-time motion planning in high-dimensional configuration spaces. In *Proc. of IEEE International Conference on Robotics and Automation*, volume 2, pages 1469–1474. IEEE, 2001. 2
- [7] Xuemin Chi, Yiming Li, Jihao Huang, Bolun Dai, Zhitao Liu, and Sylvain Calinon. Safe dynamic motion generation in configuration space using differentiable distance fields. *arXiv preprint arXiv:2412.16456*, 2024. 1, 2, 8, 9, 10
- [8] Erwin Coumans and Yunfei Bai. Pybullet, a python module for physics simulation for games, robotics and machine learning. <http://pybullet.org>, 2016–2021. 7, 9
- [9] Hongkai Dai, Alexandre Amice, Peter Werner, Annan Zhang, and Russ Tedrake. Certified polyhedral decompositions of collision-free configuration space. *The International Journal of Robotics Research*, 43(9):1322–1341, 2024. doi: 10.1177/02783649231201437. 2
- [10] Claus Danielson. Invariant configuration-space bubbles for revolute serial-chain robots. *IEEE Control Systems Letters*, 7:745–750, 2023. doi: 10.1109/LCSYS.2022.3224685. 2
- [11] Robin Deits and Russ Tedrake. *Computing Large Convex Regions of Obstacle-Free Space Through Semidefinite Programming*, pages 109–124. Springer International Publishing, Cham, 2015. ISBN 978-3-319-16595-0. doi: 10.1007/978-3-319-16595-0_7. URL https://doi.org/10.1007/978-3-319-16595-0_7. 2
- [12] E. W. Dijkstra. A note on two problems in connexion with graphs. *Numerische Mathematik*, 1:269–271, 1959. 5
- [13] Danny Driess, Jung-Su Ha, Marc Toussaint, and Russ Tedrake. Learning models as functionals of signed-distance fields for manipulation planning. In *Conference on robot learning*, pages 245–255. PMLR, 2022. 2
- [14] Peyman Mohajerin Esfahani and Daniel Kuhn. Data-driven distributionally robust optimization using the Wasserstein metric: performance guarantees and tractable reformulations. *Mathematical Programming*, 171:115–166, 2018. 6
- [15] Yarin Gal and Zoubin Ghahramani. Dropout as a bayesian approximation: Representing model uncertainty in deep learning. In *International Conference on Machine Learning*, volume 48, pages 1050–1059, 2016. 7
- [16] Emanuele Garone and Marco M Nicotra. Explicit reference governor for constrained nonlinear systems. *IEEE Transactions on Automatic Control*, 61(5):1379–1384, 2015. 6
- [17] Luxin Han, Fei Gao, Boyu Zhou, and Shaojie Shen. Festa: Fast incremental euclidean distance fields for online motion planning of aerial robots. In *2019 IEEE/RSJ International Conference on Intelligent Robots and Systems (IROS)*, pages 4423–4430, 2019. 3
- [18] Peter E. Hart, Nils J. Nilsson, and Bertram Raphael. A formal basis for the heuristic determination of minimum cost paths. *IEEE Transactions on Systems Science and Cybernetics*, 4(2):100–107, 1968. 5
- [19] Kris Hauser. Lazy collision checking in asymptotically-optimal motion planning. In *IEEE International Conference on Robotics and Automation (ICRA)*, pages 2951–2957, 2015. 2, 4, 8
- [20] John D Head and Michael C Zerner. A broyden—fletcher—goldfarb—shanno optimization procedure for molecular geometries. *Chemical physics letters*, 122(3):264–270, 1985. 3
- [21] Dan Hendrycks and Kevin Gimpel. Gaussian error linear units (gelus). *arXiv preprint arXiv:1606.08415*, 2016. 7
- [22] Michael A Johnson and Mohammad H Moradi. *PID control*. Springer, 2005. 2
- [23] Lydia E Kavraki, Petr Svestka, J-C Latombe, and Mark H Overmars. Probabilistic roadmaps for path planning in high-dimensional configuration spaces. *IEEE Transactions on Robotics and Automation (T-RO)*, 12(4):566–580, 1996. 1, 2
- [24] Shaghayegh Keyumarsi, Made Widhi Surya Atman, and Azwirman Gusrialdi. Lidar-based online control barrier function synthesis for safe navigation in unknown environments. *IEEE Robotics and Automation Letters*, 9(2): 1043–1050, 2024. 3
- [25] Mikhail Koptev, Nadia Figueroa, and Aude Billard. Neural joint space implicit signed distance functions for reactive robot manipulator control. *IEEE Robotics and Automation Letters*, 8(2):480–487, 2023. doi: 10.1109/LRA.2022.3227860. 1, 2, 3
- [26] J.J. Kuffner and S.M. LaValle. Rrt-connect: An efficient approach to single-query path planning. In *Proceedings 2000 ICRA. Millennium Conference. IEEE International Conference on Robotics and Automation. Symposia Proceedings (Cat. No.00CH37065)*, volume 2, pages 995–1001 vol.2, 2000. 2, 8
- [27] Steven M LaValle and James J Kuffner. Rapidly-exploring random trees: Progress and prospects. *Algorithmic and computational robotics*, pages 303–307, 2001. 1, 2, 4
- [28] Ki Myung Brian Lee, Zhirui Dai, Cedric Le Gentil, Lan Wu, Nikolay Atanasov, and Teresa Vidal-Calleja. Safe bubble cover for motion planning on distance fields. *arXiv preprint arXiv:2408.13377*, 2024. 2, 4, 5
- [29] Yiming Li, Xuemin Chi, Amirreza Razmjoo, and Sylvain Calinon. Configuration space distance fields for manipulation planning. In *Robotics: Science and Systems (RSS)*, 2024. 1, 2, 3, 4, 7
- [30] Yiming Li, Yan Zhang, Amirreza Razmjoo, and Sylvain Calinon. Representing robot geometry as distance fields: Applications to whole-body manipulation. In *IEEE International Conference on Robotics and Automation (ICRA)*, pages 15351–15357, 2024. 1, 2, 3

- [31] Zhichao Li, Ömür Arslan, and Nikolay Atanasov. Fast and safe path-following control using a state-dependent directional metric. In *IEEE International Conference on Robotics and Automation (ICRA)*, pages 6176–6182, 2020. 6
- [32] Kehan Long, Cheng Qian, Jorge Cortés, and Nikolay Atanasov. Learning barrier functions with memory for robust safe navigation. *IEEE Robotics and Automation Letters (RA-L)*, 6(3):4931–4938, 2021. 1, 3
- [33] Kehan Long, Hardik Parwana, Georgios Fainekos, Bardh Hoxha, Hideki Okamoto, and Nikolay Atanasov. Neural configuration distance function for continuum robot control. *arXiv preprint arXiv:2409.13865*, 2024. 3
- [34] Kehan Long, Yinzhuang Yi, Zhirui Dai, Sylvia Herbert, Jorge Cortés, and Nikolay Atanasov. Sensor-based distributionally robust control for safe robot navigation in dynamic environments. *arXiv preprint arXiv:2405.18251*, 2024. 6, 7
- [35] Helen Oleynikova, Zachary Taylor, Marius Fehr, Roland Siegwart, and Juan Nieto. Voxblox: Incremental 3d Euclidean signed distance fields for on-board MAV planning. In *IEEE/RSJ International Conference on Intelligent Robots and Systems (IROS)*, pages 1366–1373, 2017. 1
- [36] Jeong Joon Park, Peter Florence, Julian Straub, Richard Newcombe, and Steven Lovegrove. DeepSDF: Learning continuous signed distance functions for shape representation. In *IEEE/CVF Conference on Computer Vision and Pattern Recognition*, pages 165–174, 2019. 1, 3
- [37] Carlos Quintero-Peña, Wil Thomason, Zachary Kingston, Anastasios Kyrillidis, and Lydia E. Kavraki. Stochastic implicit neural signed distance functions for safe motion planning under sensing uncertainty. In *IEEE International Conference on Robotics and Automation (ICRA)*, pages 2360–2367, 2024. 1
- [38] Alexander Shkolnik and Russ Tedrake. Sample-based planning with volumes in configuration space. *arXiv preprint arXiv:1109.3145*, 2011. 2
- [39] Andrew Singletary, William Guffey, Tamas G. Molnar, Ryan Sinnet, and Aaron D. Ames. Safety-critical manipulation for collision-free food preparation. *IEEE Robotics and Automation Letters*, 7(4):10954–10961, 2022. 1, 2
- [40] Vincent Sitzmann, Julien Martel, Alexander Bergman, David Lindell, and Gordon Wetzstein. Implicit neural representations with periodic activation functions. In *International Conference on Neural Information Processing Systems (NeurIPS)*, volume 33, pages 7462–7473, 2020. 1
- [41] Ioan A. Şucan, Mark Moll, and Lydia E. Kavraki. The Open Motion Planning Library. *IEEE Robotics & Automation Magazine*, 19(4):72–82, December 2012. doi: 10.1109/MRA.2012.2205651. <https://ompl.kavrakilab.org>. 8
- [42] Vasileios Vasilopoulos, Suveer Garg, Pedro Piacenza, Jinwook Huh, and Volkan Isler. Ramp: Hierarchical reactive motion planning for manipulation tasks using implicit signed distance functions. In *IEEE/RSJ International Conference on Intelligent Robots and Systems (IROS)*, pages 10551–10558, 2023. 2
- [43] Kun Wei and Bingyin Ren. A method on dynamic path planning for robotic manipulator autonomous obstacle avoidance based on an improved RRT algorithm. *Sensors*, 18(2):571, 2018. 1
- [44] Peter Werner, Thomas Cohn, Rebecca H Jiang, Tim Seyde, Max Simchowitz, Russ Tedrake, and Daniela Rus. Faster algorithms for growing collision-free convex polytopes in robot configuration space. *arXiv preprint arXiv:2410.12649*, 2024. 2
- [45] Libo Yang and S.M. LaValle. The sampling-based neighborhood graph: an approach to computing and executing feedback motion strategies. *IEEE Transactions on Robotics and Automation*, 20(3):419–432, 2004. doi: 10.1109/TRA.2004.824640. 2
- [46] Mingxin Yu, Chenning Yu, M-Mahdi Naddaf-Sh, Devesh Upadhyay, Sicun Gao, and Chuchu Fan. Efficient motion planning for manipulators with control barrier function-induced neural controller. In *2024 IEEE International Conference on Robotics and Automation (ICRA)*, pages 14348–14355, 2024. 2, 3
- [47] Xiankun Zhu, Yucheng Xin, Shoujie Li, Houde Liu, Chongkun Xia, and Bin Liang. Efficient collision detection framework for enhancing collision-free robot motion. *arXiv preprint arXiv:2409.14955*, 2024. 1, 2, 8, 9, 10